Investigation of the Octahedral Network Structure in Formamidinium Lead Bromide Nanocrystals by Low-Dose Scanning Transmission Electron Microscopy

Nadine J. Schrenker[1,2], Tom Braeckevelt[3,4], Annick De Backer[1,2], Nikolaos Livakas[5,6], Chu-Ping Yu[1,2], Thomas Friedrich[1,2], Maarten B.J. Roeffaers[7], Johan Hofkens[4], Johan Verbeeck[1,2], Liberato Manna[5], Veronique Van Speybroeck[3], Sandra Van Aert[1,2,], Sara Bals[1,2,]**

1 Electron Microscopy for Materials Science (EMAT), University of Antwerp, 2020 Antwerp, Belgium

2 NANOlab Center of Excellence, University of Antwerp, 2020 Antwerp, Belgium

3 Center for Molecular Modeling, Ghent University, 9052 Zwijnaarde, Belgium

4 Department of Chemistry, KU Leuven, 3001 Leuven, Belgium

5 Department of Nanochemistry, Istituto Italiano di Tecnologia (IIT), 16163 Genova, Italy

6 Dipartimento di Chimica e Chimica Industriale, Università di Genova, 16146 Genova, Italy

7 cMACS, Department of Microbial and Molecular Systems, KU Leuven, 3001 Leuven, Belgium

*Corresponding authors: sandra.vanaert@uantwerpen.be, sara.bals@uantwerpen.be

ABSTRACT: Metal halide perovskites (MHP) are highly promising semiconductors. In this study, we focus on $FAPbBr_3$ nanocrystals, which are of great interest for green light-emitting diodes. Structural parameters significantly impact the properties of MHPs and are linked to the phase instability, which is hampering long-term applications. Clearly, there is a need for local and precise characterization techniques at the atomic scale, such as transmission electron microscopy. Due to the high electron beam sensitivity of MHPs, these investigations are extremely challenging. Here, we applied a low-dose method based on four-dimensional scanning transmission electron microscopy. We quantified the observed elongation of the projections of the Br atomic columns, suggesting an alternation in the position of the Br atoms perpendicular to the Pb-Br-Pb bonds. Together with molecular dynamics simulations, these results remarkably reveal local distortions in an on-average cubic structure. Additionally, this study provides an approach to prospectively investigate fundamental degradation mechanisms of MHP.

KEYWORDS: 4D-STEM, transmission electron microscopy, hybrid organic-inorganic metal halide perovskites, neural network, octahedral tilt, molecular dynamics

Hybrid organic-inorganic metal halide perovskites are highly promising semiconductors for novel optoelectronic devices, including photovoltaics, light-emitting diodes (LEDs) or X-ray detectors.[1,2] Their excellent optoelectronic properties, e.g. a tunable bandgap, high charge carrier mobility, high photoluminescence quantum yield (PLQY) and low recombination rate of photogenerated carriers, are the reason for their rapid evolution.[2,3] The structure of metal halide perovskites (MHP) is described by the chemical formula ABX_3, where A is a monovalent organic cation (e.g. formamidinium (FA^+) [$CH(NH_2)_2^+$] or methylammonium (MA^+) [$CH_3NH_3^+$]) or a metal cation (e.g. Cs^+), B is a divalent metal cation (typically Pb^{2+}or Sn^{2+}), and X is a halide anion (X = Cl^-, Br^-, I^-).[4,5] Generally, the central B-metal cation is octahedrally coordinated with six halides, i.e. $[BX_6]^{4-}$. The octahedra form a three-dimensional connected network through the corner halides. Orbitals of the B-ions hybridize with orbitals from the halide ions to form the conduction and valence band.[2,4] Therefore, the position of the valence band is sensitive to the choice of both the B-ion and the halide ion. Focusing on the halide, the band gap generally increases from I^- to Br^- to Cl^- and can be finely tuned by mixing halides.[6] The A-site cations fill the cuboctahedral voids in the perovskite structure.[4] Thus, the band structure is indirectly influenced by A-site cations, since they affect the bond length and angle between the B- and X-site ions, i.e. through steric interactions or by octahedral tilting.[7,8] The re-orientational dynamics of A-cations, in particular organic cations, influences the tilting of the $[BX_6]^{4-}$ octahedra,[4,9] but the effect of motion and polarity of cations on ion migration and charge carrier dynamics is still under debate.[9] Nevertheless, it is apparent that structural parameters, such as octahedral tilting, have significant impact on the optical and electronic properties of MHPs.[7,9] Another aspect closely linked with the octahedral network structure is the polymorphic nature of MHPs, which is of great importance since phase instability is still one of the major roadblocks for long-term applications

of MHPs. Indeed, for lead iodide-based compositions, only the "black" phase demonstrates photoactive properties, which dramatically decrease once the MHPs convert to the "yellow" phase.[10–13] The black phase includes the cubic, orthorhombic, and tetragonal phase. From the high-symmetry cubic ($Pm\bar{3}m$, No. 221) phase, the transition to the lower symmetry phases can be described by rotation or shearing of the octahedra.[14–16] The tetragonal phase (P4/mbm, No. 127) shows an in-phase rotation of the $[BX_6]^{4-}$ octahedral network about the c-axis,[17] whereas in the orthorhombic phase (Pnma, No.62) the octahedra show an out-of-phase rotation.[18] In the yellow phase, the crystal structure changes and instead of corner-sharing octahedra the structure consists of face-sharing or edge-sharing octahedra.[19] In this study, we focus on hybrid organic-inorganic $FAPbBr_3$ nanocrystals (NCs), which are of great interest for green light-emitting diodes because these NCs show a bright and stable emission at around 530 nm. Moreover, the PL exhibits a high color purity due to narrow emission linewidth and PLQY of > 95 %.[20,21] However, the lack of long-term stability of MHPs is hampering their implementation in commercial applications.[10,12] Understanding the role of the octahedral network to further establish the structure-property connection and its transformation during degradation is therefore of great importance.

Using advanced X-ray techniques, the unit cell parameters, the space group and phase transformations under *in situ* conditions can be precisely determined.[22] However, these techniques provide only averaged information and lack the ability to probe more local structural details. Transmission electron microscopy (TEM) is a very powerful technique to measure the local structure of NCs, even at atomic resolution. However, in the case of MHPs it comes along with the challenge of a high sensitivity to the electron beam.[2] Irradiation with the electron beam easily causes degradation of the MHP NCs with PbX_2 and Pb as resulting products.[23,24] To study subtle changes, such as octahedral tilting, the effect of the electron beam should be taken into account,

especially for hybrid organic-inorganic MHPs that inherently yield a higher sensitivity to the electron beam than their fully inorganic counterparts due to the presence of organic cations.[25,26]

High-angle annular dark-field (HAADF) scanning TEM (STEM) imaging is a common technique to investigate MHPs,[27–29] but a relatively high electron dose is required. Several alternative imaging techniques have been reported with the aim to mitigate the effect of electron beam damage, including cryogenic conditions and exit wave reconstruction.[25,30] The phase of the exit wave is proportional to the projected electrostatic potential of the structure [31] and phase images are therefore more sensitive to light elements. Compared to HAADF-STEM imaging, in which the intensity scales roughly with the atomic number $Z^{1.7}$, phase imaging is preferred when imaging MHP materials in which both heavy and light elements are present simultaneously.[32] A promising phase contrast imaging technique is based on the concept of 4D-STEM, where a convergent beam electron diffraction (CBED) pattern is collected for every scan position.[33,34] It has been shown that deviations of the center of mass (COM) in these diffraction patterns are directly related to the electrostatic potential field, resulting in images that linearly depend on the atomic number Z. Moreover, all electrons are collected by a hybrid pixelated direct electron detector, whereas in HAADF-STEM only electrons scattered to relatively high angles are used. 4D-STEM is, therefore, superior with respect to information richness and dose-efficiency as compared to HAADF-STEM. There are several approaches to extract the phase from a 4D-STEM dataset. Ptychographic methods have been of particular interest for their super-resolution capabilities and the possibility to determine/correct for microscope aberrations as well. However, the computational cost and memory requirements for these algorithms are considerable.

In the present work, we explore the application of machine learning (ML) [35,36] for reconstructing phase images of $FAPbBr_3$ NCs from low-dose 4D-STEM data with super-resolution in (near) real

time.[33,35] This approach allowed us to visualize the light FA and Br atomic columns even at electron doses below 50 $e^-/Å^2$. Moreover, we were able to perform a quantitative analysis of the octahedral network structure as a function of electron dose, which was further interpreted based on molecular dynamics (MD) simulations. This correlative analysis suggested an anisotropic displacement of the Br anions, which leads to local distortions in an on-average cubic structure.

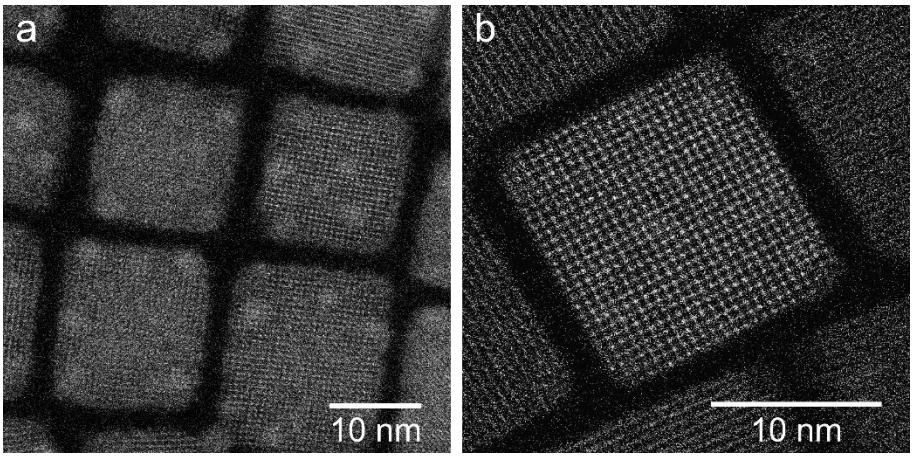

Figure 1. HAADF-STEM imaging of $FAPbBr_3$ NCs. The electron dose for imaging was ~ 300 $e^-/Å^2$ in panel (a) and ~ 40 $e^-/Å^2$ in panel (b). In panel (a) the formation of Pb-rich clusters due to the electron beam irradiation is visible.

Colloidal $FAPbBr_3$ NCs were synthesized following a hot injection method as previously reported [37], which delivered monodispersed cubic-shaped NCs samples with a PL maximum at 530 nm (see S1, method section for details). The $FAPbBr_3$ NCs are imaged by HAADF-STEM in **Figure 1**, which reveals that the NCs have a cubic morphology and their size is about 15 – 20 nm. The total electron dose used for imaging in **Figure 1**a was ~ 300 $e^-/Å^2$. This relatively high dose leads to Pb-rich clusters as a consequence of radiolysis[2,23], which can be observed as bright particles in **Figure 1**a. To reduce the effect of electron beam damage, we lowered the total electron dose to ~ 40 $e^-/Å^2$ (**Figure 1**b), which is in accordance with the dose recommendation for hybrid organic-inorganic perovskites by Rothmann et al.[38]. Although this electron dose reduction overcomes the formation of the Pb-rich clusters, only the heavy Pb atomic columns are clearly detectable in the HAADF image, whereas the nearby light elements, such as Br or C, that scatter less, are hardly invisible.

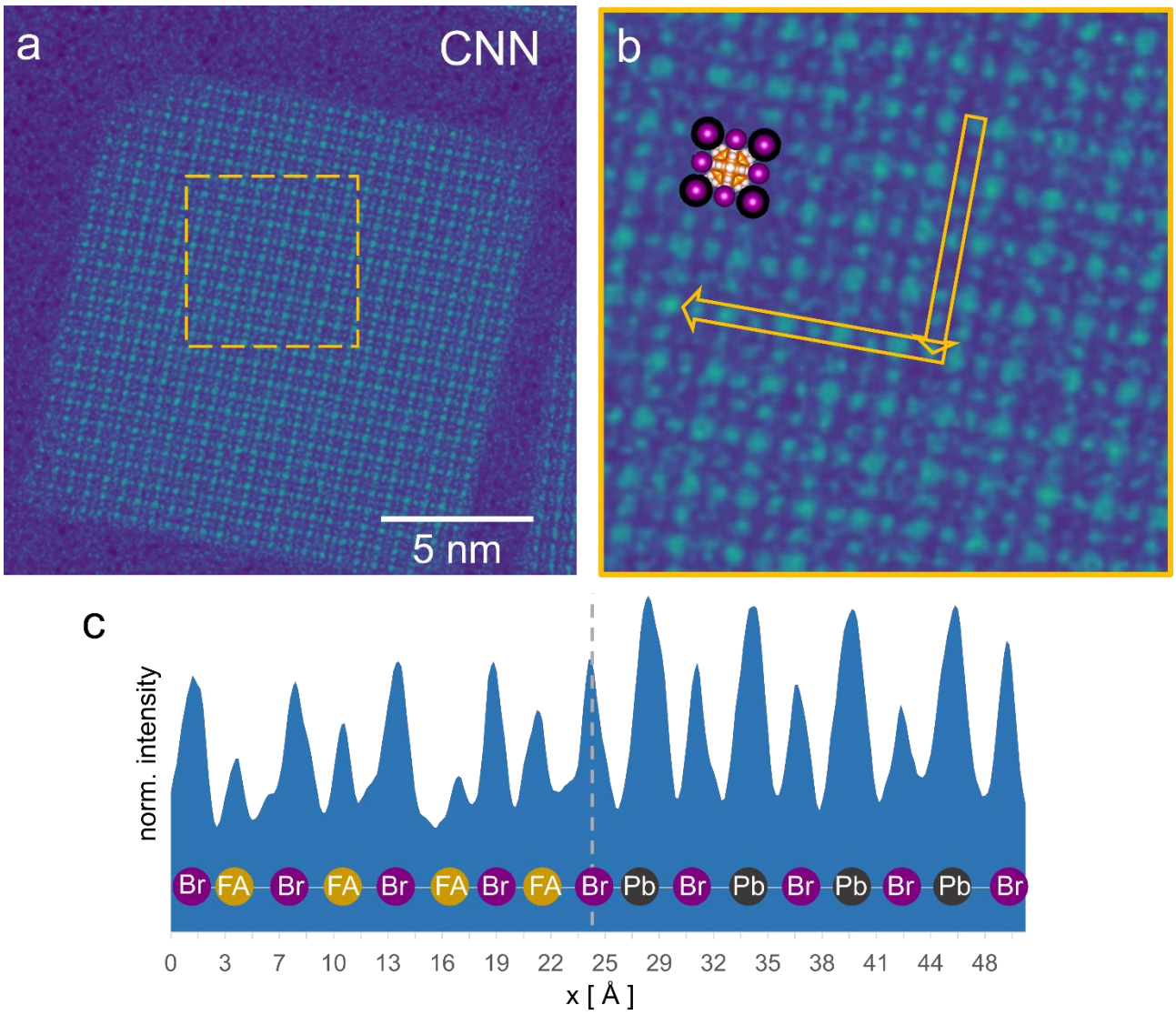

Figure 2. High-resolution imaging of $FAPbBr_3$ NCs. (a) CNN reconstructions were applied to obtain the high-resolution image of a $FAPbBr_3$ NC from a 4D-STEM dataset. The total electron dose is ~ 48 $e^-/Å^2$. (b) Enlarged image corresponding to the area indicated by a rectangle in panel (a). The overlay indicates the unit cell (Br = purple, Pb = black, FA = orange). (c) The line profiles, which were taken along the direction of the arrows in panel (b), where the vertical line is along the Br-FA columns and the horizontal line along the Br-Pb columns, show that in the CNN reconstruction Pb, Br and FA can be distinguished from their intensity.

To overcome this limitation, we here applied 4D-STEM in combination with a recently developed convolutional neural network (CNN). The phase reconstruction can be considered as an inverse problem, which is here solved for every scan point based on a set of diffraction patterns (3x3 kernel) of overlapping probe positions by means of CNNs.[33] The CNN was trained based on a large synthetic dataset, using atomic structures extracted from the materials project database (www.materialsproject.org).[39] The CNN reconstruction of a $FAPbBr_3$ NC is shown in **Figure 2**a. The total electron dose for the dataset was equal to 48 e^-/A^2. From this figure, it is clear that the CNN reconstruction enables to visualize these beam-sensitive NCs with an electron dose that is sufficiently low to avoid the formation of Pb-rich clusters due to electron beam irradiation, while maintaining a high signal-to-noise ratio (SNR) (see S3). It should be emphasized that, in contrast to the HAADF-STEM images, the CNN reconstruction reveals all atomic columns, including the FA and Br columns, which can be distinguished from their intensity in the line profile (see **Figure 2**b,c). Close inspection of the Br columns indicates deviations from perfect round projections. This observation suggests an alternation in the position of the Br atoms along the viewing direction (see projected images of the $FAPbBr_3$ unit cell in S4), which directly affects the $[PbBr_6]^{4-}$ octahedral network within the NCs. As mentioned before, the octahedral tilt and the Pb-Br-Pb bond angle serve as a crucial indicator for the phase stability and can change upon doping or degradation due to environmental triggers.

To determine the shape of the projections of the atomic columns in more detail, we applied an averaging process to the 4D-STEM dataset of a single NC, as explained in the methods section (see S6, S7, template matching section in SI). In short, we assumed perfect crystal periodicity, CBED patterns from equivalent lattice positions, which were added to obtain an averaged 4D-STEM dataset that could be used as input for the CNN reconstruction (see **Figure 3**a). Next, we

applied statistical parameter estimation theory (see Ref. [40,41]) to **Figure 3**a to measure deviations from perfectly circular projections of atomic columns. For this purpose, a parametric model consisting of a sum of 2D elliptical Gaussians, each centered on the atomic column positions, was used (see Figure S5). The unknown parameters, i.e. the positions and the width along the major and minor axes, were estimated by fitting this model to the CNN reconstruction using a non-linear least squares optimization.[41,42] In **Figure 3**b, the model resulting from the fitting is presented. The arrows within the figure indicate the ellipticity ratio of the projections of the Br atomic columns. In a perfectly cubic structure, the $[PbBr_6]^{4-}$ octahedra are not tilted (see S4) and hence, the value for the ellipticity ratio, defined as the ratio of the major to minor axis, is expected to be one. However, for the analyzed $FAPbBr_3$ NC, the median of the ellipticity ratio of the projections of the Br atomic columns was found to be 1.28 ± 0.01. Moreover, additional datasets on the analysis of the ellipticity ratio are presented in S8. The deviation from 1 is possibly related to an alternation in the position, due to thermal motion, of the Br atoms along the viewing direction, as schematically illustrated in **Figure 3**b and **Figure 3**c. This might be related to a small degree of flexibility in the octahedral network structure. In this case, the Br atoms can be displaced perpendicular to the Pb-Br-Pb bond. Due to the ionic nature, the bond between Pb^{2+} and Br^- ions is much stronger than the bond of the organic FA-cations to the surrounding $[PbBr_6]^{4-}$ octahedra through hydrogen bondings.[9,42,43] Another possible explanation is that the octahedra in the perovskite structure have a small, fixed tilt, which would, however, lead to a deviation of the $Pm\bar{3}m$ cubic structure. As XRD measurements and Rietveld refinement (see S2) for the investigated $FAPbBr_3$ NCs agree best with the cubic structure, the observed ellipticity is likely the result of a slight deviations of Br atoms from their ideal positions, as described by the first explanation. These results are in good agreement with previous synchrotron XRD measurements

of $FAPbBr_3$ NC, where the measured Pb-Br-Pb bond angles deviate by up to 15 ° from the ideal 180 ° angle due to local disorder caused by displacement of Br anions, while the average structure is cubic and no superstructure peaks were observed.[21,43] Via the "split cubic" model,[21,43] where displacements of the Br anions perpendicular to the Pb-Br-Pb bonds are considered, the measured XRD patterns and peak intensities could be fitted well. Also in other recent reports, for different types of MHPs similar anisotropic displacements and dynamics of the halide ions were observed.[42,44]

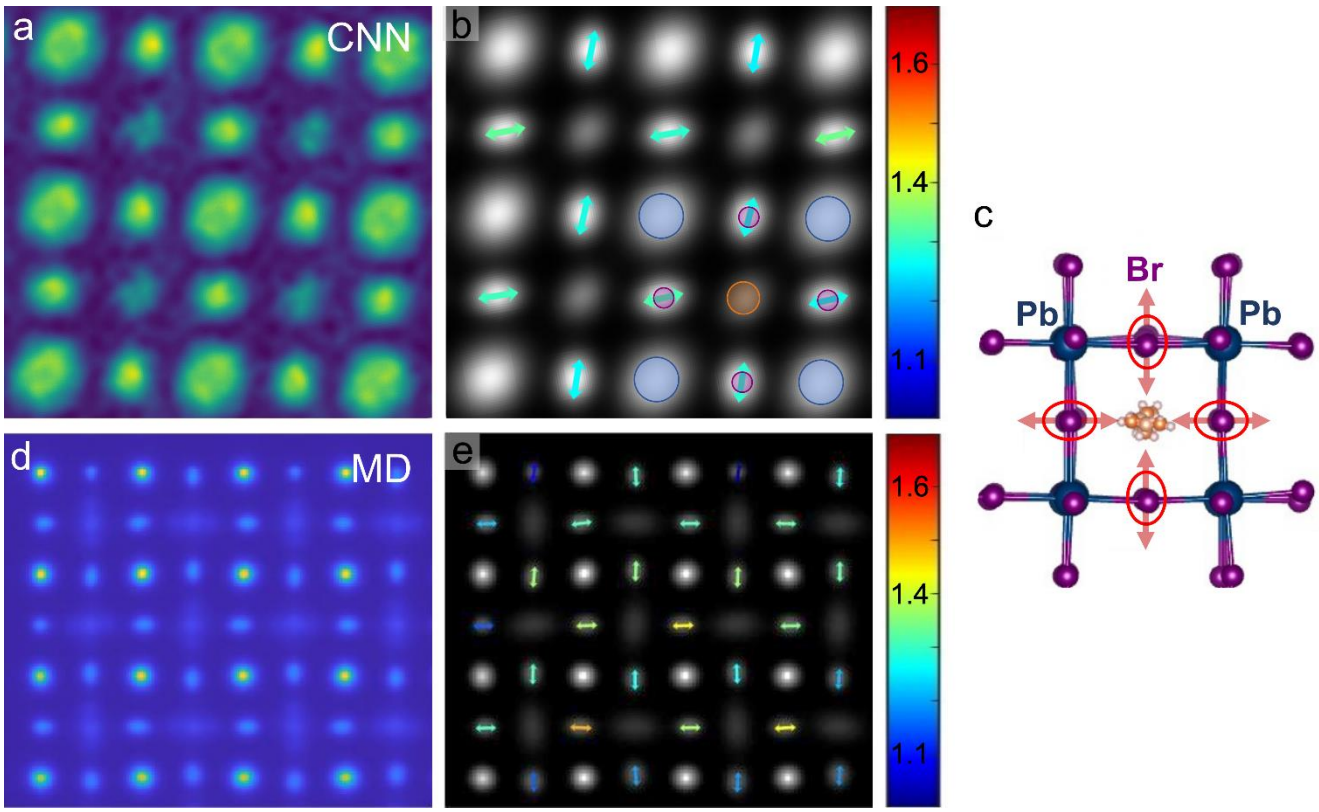

Figure 3. Octahedral network in $FAPbBr_3$ NCs. (a) CNN reconstruction of a $FAPbBr_3$ NCs. The 4D-STEM data of the NC depicted in Figure 2a was averaged via template matching. (b) The obtained model after fitting elliptical Gaussian peaks to the atomic columns in the CNN reconstruction of panel (a). The color bar represents the ellipticity ratio of the projections of the Br atomic columns. The overlay indicates the different atomic columns (Br = purple, Pb-Br = blue, FA = orange). (c) Schematic illustration of a $FAPbBr_3$ structure, where the Br anions contain a small displacement perpendicular to the Pb-Br-Pb bond, as indicated by the red arrows. The red ellipses show the exemplary position of the Br atomic columns that are analyzed in panel (b). (d) Simulated image of the projected electrostatic potential of the $FAPbBr_3$ structure at 300 K and atmospheric pressure obtained via MD simulations. (e) The obtained model after fitting elliptical Gaussian peaks to the simulated image shown in panel (d). The arrows indicate the ellipticity ratio of the projections of the Br atomic columns.

To understand if the observed displacement of the Br anions in $FAPbBr_3$ NCs would be a result of electron beam illumination, a series of MD simulations of 250 ps were performed using a machine learning potential (MLP) trained on underlying Density Functional Theory (DFT) energies and forces (more computational details are given in the methods section). The temperature and pressure were controlled during the MD simulation and set to 300 K and 0.1 MPa, respectively. The MLP makes it possible to increase the time scale of MD simulations performed with DFT from a few picoseconds to hundreds of picoseconds. After averaging the structure over 200 ps, a cubic structure, with slightly displaced Br positions, is obtained. This input structure was used for image simulations using the MULTEM software[45] to compare our 4D-STEM experiments with the MD simulations. During the MULTEM image simulations, the projected electrostatic potential is calculated and considered to be the equivalent of the phase object reconstruction, which is obtained via CNNs in the experiment.[33] For these image simulations, one snapshot every 50 fs was selected from the last 200 ps of the MD simulations. After averaging the simulated images of the projected electrostatic potential of each snapshot (see **Figure 3**d), a model of 2D elliptical Gaussian peaks was fitted (**Figure 3**e). The median of the ellipticity ratio of the projections of the Br atomic columns was determined as 1.30 ± 0.03. These results are in good agreement with the values obtained via low-dose 4D-STEM measurements (see **Figure 3**a-b, **Table 1**). The comparison between the experiments and the MD simulation shows that, at the electron doses used, the electron beam does not affect the observed ellipticity. Moreover, the locally distorted structure (see S9), which is cubic on-average, is caused by an inherent anisotropic displacement of the Br anions.

We also analyzed a $FAPbBr_3$ NC with an increased total electron dose of 144 $e^-/Å^2$ (see S10). In this case, the median of the ellipticity ratio of the projections of the Br atomic columns was

determined as 1.43 ± 0.04, which is a significant increase compared to the low-dose 4D-STEM data shown in **Figure 3**. Electron beam irradiation can lead to degradation of MHP NCs through the loss of halide ions and organic cations,[38,46] meaning that vacancies are expected to increase upon electron beam irradiation. To understand if the increased ellipticity is related to the presence of vacancies and therefore beam damage, we compared the experimental observations with MD simulations that contain vacancies in the perovskite structure. Following the same approach as explained above, the ellipticity ratio was measured as a function of increasing number of FABr vacancies, i.e. the loss of cation/anion (FA^+ and Br^-) pairs (see S11). In the MD simulations the FABr vacancies are randomly distributed, assuming no ordered structure of vacancies is induced. The determined average Pb-Br-Pb angle (see S11) slightly decreases with increasing number of vacancies, which correlates with more mobile Br^- anions. For randomly distributed vacancies, the median of the ellipticity ratio determined for the projections of the Br atomic columns showed no significant increase with increasing number of vacancies. However, the standard error of the median increased for the MD simulations with vacancies as well as for the TEM experiment with increased electron dose, which indicates a more disordered structure due to mobile Br^- anions. It can therefore be hypothesized that other effects, such as a higher energy transfer from the impinging electron beam to the sample, further increase the mobility of the Br^- anions. Alternatively, a more complex ordered vacancy structure and rotation of the $[PbBr_6]^{4-}$ octahedra may also contribute to the observed increase in ellipticity ratio. We suggest that the investigation of the ellipticity ratio of the atomic columns at low electron doses is a valuable approach for studying phase changes and degradation of MHP NCs, for instance caused by environmental triggers, at a local scale.

Table 1. The ellipticity ratio of the projections of the Br atomic columns. For each fit the median and the standard error of the median is given.

	Low-dose ($48\ e^-/A^2$) 4D-STEM	Increased dose ($144\ e^-/A^2$) 4D-STEM	MD simulation pristine structure (200ps)	MD simulation 11 FABr vacancies (200 ps)
Br	1.28 ± 0.01	1.43 ± 0.04	1.30 ± 0.03	1.32 ± 0.04

In conclusion, we have demonstrated an approach to apply low-dose 4D-STEM imaging to the quantitative analysis of $FAPbBr_3$ NCs. To retrieve phase contrast imaging from 4D-STEM datasets, we utilize the capacity of machine learning. In the CNN reconstructions, the different atomic columns in the perovskite structure could be detected and remarkably, it was also possible to clearly distinguish the light FA cations and the Br atomic columns from the image intensity. To analyze the octahedral network structure, we determined the shape of the projections of the atomic columns via a parametric model, which consists of a sum of 2D elliptical Gaussians, each centered on the atomic column positions. The analysis of 4D-STEM datasets of $FAPbBr_3$ NCs and MD simulations revealed an elongation of the projections of the Br atomic columns. This is caused by an anisotropic displacement of the Br anions perpendicular to the Pb-Br-Pb bonds, causing local distortions in an on-average cubic crystal structure. The presented technique enables the analysis of the octahedral network in MHPs at a local scale. Furthermore, since it can be transferred to *in situ* TEM experiments, this study provides an approach to prospectively investigate fundamental degradation mechanisms of MHP NCs under environmental triggers.

ABSTRACT GRAPHIC

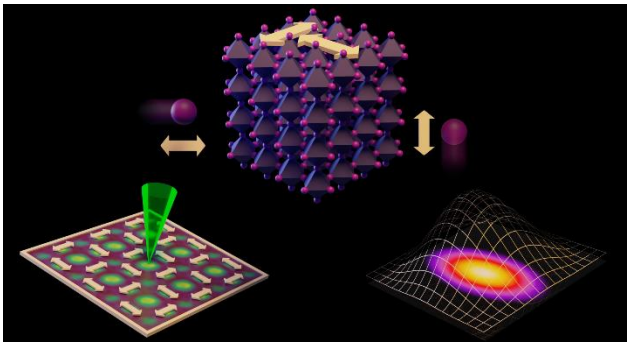

ASSOCIATED CONTENT

Supporting Information

The Supporting Information is available free of charge at DOI:

Materials and methods, optical properties of $FAPbBr_3$ NCs, structural characterization via X-ray diffraction, refined parameters of the $FAPbBr_3$ structural model, overview CNN images of the $FAPbBr_3$ NCs, illustration of the $FAPbBr_3$ structure in projection, elliptical fitting of the projections of the atomic columns using a parametric model, template matching for low-dose and increased dose 4D-STEM dataset, additional datasets for the analysis of the ellipticity ratio, snapshots of MD simulations of $FAPbBr_3$ along different orientations, influence of electron dose on the structure of $FAPbBr_3$ NCs, MD simulations on the influence of FA^+ and Br^- vacancies on the structure of $FAPbBr_3$

AUTHOR INFORMATION

Corresponding Author

* Sandra Van Aert – Email : sandra.vanaert@uantwerpen.be, Sara Bals – Email :

sara.bals@uantwerpen.be,

Author Contributions

N.J.S. performed and analyzed the STEM experiments. T.B. conducted MD simulations. N.L. synthesized the NCs and performed characterization via optical spectroscopy and XRD. C.Y. and T.F. developed the CNN reconstruction method. A.D.B. contributed to the analysis via the parametric imaging model and the MULTEM simulations. M.R., J.H., V.V.S., L.M., J.V., S.V.A. and S.B. coordinated the research work. N.J.S., S.V.A. and S.B. wrote the manuscript. All authors contributed to reviewing and editing the manuscript and have given approval to the final version of the manuscript.

Funding Sources

Any funds used to support the research of the manuscript should be placed here (per journal style).

ACKNOWLEDGMENT

The authors acknowledge financial support from the Research Foundation – Flanders (FWO) through project fundings (G0A7723N) and a postdoctoral fellowship to N.J.S. (FWO Grant No. 1238622N, V413524N). The authors acknowledge financial support from iBOF-21-085 PERSIST. S.B. and S.V.A. acknowledge financial support from the European Commission by ERC Consolidator grant no. 815128 (REALNANO) and grant no. 770887 (PICOMETRICS). L.M. acknowledges financial support from the European Commission by ERC Advanced grant no. 101095974 (NEHA). V.V.S. furthermore acknowledges the Research Fund of Ghent University (BOF) for its financial support. The computational resources and services used in this work were provided by VSC (Flemish Supercomputer Center), funded by the Research Foundation-Flanders (FWO), and the Flemish Government.

ABBREVIATIONS

Convergent beam electron diffraction CBED, convolutional neural network CNN, center of mass COM, density functional theory DFT, formamidinium lead tribromide $FAPbBr_3$, high-angle annular dark-field HAADF, light-emitting diode LED, MHP metal halide perovskites, machine learning ML, machine learning potential MLP, molecular dynamics MD, NC nanocrystals, photoluminescence PL, photoluminescence quantum yield PLQY, real-time integration COM riCOM, signal-to-noise ratio SNR, scanning transmission electron microscopy STEM, X-ray powder diffraction XRPD

REFERENCES

(1) Huang, H.; Pradhan, B.; Hofkens, J.; Roeffaers, M. B. J. J.; Steele, J. A. Solar-Driven Metal Halide Perovskite Photocatalysis: Design, Stability, and Performance. *ACS Energy Lett* **2020**, *5* (4), 16. https://doi.org/10.1021/acsenergylett.0c00058.

(2) Dey, A.; Ye, J.; De, A.; Debroye, E.; Ha, S. K.; Bladt, E.; Kshirsagar, A. S.; Wang, Z.; Yin, J.; Wang, Y.; Quan, L. N.; Yan, F.; Gao, M.; Li, X.; Shamsi, J.; Debnath, T.; Cao, M.; Scheel, M. A.; Kumar, S.; Steele, J. A.; Gerhard, M.; Chouhan, L.; Xu, K.; Wu, X.; Li, Y.; Zhang, Y.; Dutta, A.; Han, C.; Vincon, I.; Rogach, A. L.; Nag, A.; Samanta, A.; Korgel, B. A.; Shih, C.-J.; Gamelin, D. R.; Son, D. H.; Zeng, H.; Zhong, H.; Sun, H.; Demir, H. V.; Scheblykin, I. G.; Mora-Seró, I.; Stolarczyk, J. K.; Zhang, J. Z.; Feldmann, J.; Hofkens, J.; Luther, J. M.; Pérez-Prieto, J.; Li, L.; Manna, L.; Bodnarchuk, M. I.; Kovalenko, M. V.; Roeffaers, M. B. J.; Pradhan, N.; Mohammed, O. F.; Bakr, O. M.; Yang, P.; Müller-Buschbaum, P.; Kamat, P. V.; Bao, Q.; Zhang, Q.; Krahne, R.; Galian, R. E.; Stranks, S. D.; Bals, S.; Biju, V.; Tisdale, W. A.; Yan, Y.; Hoye, R. L. Z.; Polavarapu, L. State of the Art and Prospects for Halide Perovskite Nanocrystals. *ACS Nano* **2021**, *15* (7), 10775–10981. https://doi.org/10.1021/acsnano.0c08903.

(3) Jeong, J.; Kim, M.; Seo, J.; Lu, H.; Ahlawat, P.; Mishra, A.; Yang, Y.; Hope, M. A.; Eickemeyer, F. T.; Kim, M.; Yoon, Y. J.; Choi, I. W.; Darwich, B. P.; Choi, S. J.; Jo, Y.; Lee, J. H.; Walker, B.; Zakeeruddin, S. M.; Emsley, L.; Rothlisberger, U.; Hagfeldt, A.; Kim, D. S.; Grätzel, M.; Kim, J. Y. Pseudo-Halide Anion Engineering for α-$FAPbI_3$ Perovskite Solar Cells. *Nature* **2021**, *592* (7854), 381–385. https://doi.org/10.1038/s41586-021-03406-5.

(4) Byranvand, M. M.; Otero-Martínez, C.; Ye, J.; Zuo, W.; Manna, L.; Saliba, M.; Hoye, R. L. Z.; Polavarapu, L. Recent Progress in Mixed A-Site Cation Halide Perovskite Thin-Films and Nanocrystals for Solar Cells and Light-Emitting Diodes. *Adv Opt Mater* **2022**, *10* (14), 2200423. https://doi.org/10.1002/ADOM.202200423.

(5) Ha, S. T.; Su, R.; Xing, J.; Zhang, Q.; Xiong, Q. Metal Halide Perovskite Nanomaterials: Synthesis and Applications. *Chem Sci* **2017**, *8* (4), 2522–2536. https://doi.org/10.1039/C6SC04474C.

(6) Otero-Martínez, C.; Imran, M.; Schrenker, N. J.; Ye, J.; Ji, K.; Rao, A.; Stranks, S. D.; Hoye, R. L. Z.; Bals, S.; Manna, L.; Pérez-Juste, J.; Polavarapu, L. Fast A-Site Cation Cross-Exchange at Room Temperature: Single-to Double- and Triple-Cation Halide Perovskite Nanocrystals. *Angew Chem Int Edit* **2022**, *61* (34), e202205617. https://doi.org/10.1002/ANIE.202205617.

(7) Filip, M. R.; Eperon, G. E.; Snaith, H. J.; Giustino, F. Steric Engineering of Metal-Halide Perovskites with Tunable Optical Band Gaps. *Nat Commun* **2014**, *5* (1), 1–9. https://doi.org/10.1038/ncomms6757.

(8) Doherty, T. A. S.; Nagane, S.; Kubicki, D. J.; Jung, Y. K.; Johnstone, D. N.; Iqbal, A. N.; Guo, D.; Frohna, K.; Danaie, M.; Tennyson, E. M.; Macpherson, S.; Abfalterer, A.; Anaya, M.; Chiang, Y. H.; Crout, P.; Ruggeri, F. S.; Collins, S. M.; Grey, C. P.; Walsh, A.; Midgley, P. A.; Stranks, S. D. Stabilized Tilted-Octahedra Halide Perovskites Inhibit Local Formation of Performance-Limiting Phases. *Science* **2021**, *374* (6575), 1598–1605. https://doi.org/10.1126/SCIENCE.ABL4890.

(9) Lee, J. W.; Tan, S.; Seok, S. Il; Yang, Y.; Park, N. G. Rethinking the A Cation in Halide Perovskites. *Science* **2022**, *375* (6583). https://doi.org/10.1126/SCIENCE.ABJ1186.

(10) Saliba, M.; Matsui, T.; Seo, J. Y.; Domanski, K.; Correa-Baena, J. P.; Nazeeruddin, M. K.; Zakeeruddin, S. M.; Tress, W.; Abate, A.; Hagfeldt, A.; Grätzel, M. Cesium-Containing Triple Cation Perovskite Solar Cells: Improved Stability, Reproducibility and High Efficiency. *Energy Environ Sci* **2016**, *9* (6), 1989–1997. https://doi.org/10.1039/C5EE03874J.

(11) Steele, J. A.; Solano, E.; Jin, H.; Prakasam, V.; Yuan, H.; Lin, Z.; Wang, Q.; Chernyshov, D.; Hofkens, J.; Roeffaers, M. B. J. Texture Formation in Polycrystalline Thin Films of All-Inorganic Lead Halide Perovskite. *Adv Mater* **2020**, *2021*, 2007224. https://doi.org/10.1002/adma.202007224.

(12) Steele, J. A.; Braeckevelt, T.; Prakasam, V.; Degutis, G.; Yuan, H.; Jin, H.; Solano, E.; Puech, P.; Basak, S.; Pintor-Monroy, M. I.; Van Gorp, H.; Fleury, G.; Yang, R. X.; Lin, Z.; Huang, H.; Debroye, E.; Chernyshov, D.; Chen, B.; Wei, M.; Hou, Y.; Gehlhaar, R.; Genoe, J.; De Feyter, S.; Rogge, S. M. J.; Walsh, A.; Sargent, E. H.; Yang, P.; Hofkens, J.; Van Speybroeck, V.; Roeffaers, M. B. J. An Embedded Interfacial Network Stabilizes Inorganic $CsPbI_3$ Perovskite Thin Films. *Nat Commun* **2022**, *13* (1), 1–11. https://doi.org/10.1038/s41467-022-35255-9.

(13) Steele, J. A.; Jin, H.; Dovgaliuk, I.; Berger, R. F.; Braeckevelt, T.; Yuan, H.; Martin, C.; Solano, E.; Lejaeghere, K.; Rogge, S. M. J.; Notebaert, C.; Vandezande, W.; Janssen, K. P. F.; Goderis, B.; Debroye, E.; Wang, Y. K.; Dong, Y.; Ma, D.; Saidaminov, M.; Tan, H.; Lu, Z.; Dyadkin, V.; Chernyshov, D.; Van Speybroeck, V.; Sargent, E. H.; Hofkens, J.; Roeffaers, M. B. J. Thermal Unequilibrium of Strained Black $CsPbI_3$ Thin Films. *Science* **2019**, *365* (6454), 679–684. https://doi.org/10.1126/science.aax3878.

(14) Lee, J. W.; Seo, S.; Nandi, P.; Jung, H. S.; Park, N. G.; Shin, H. Dynamic Structural Property of Organic-Inorganic Metal Halide Perovskite. *iScience* **2021**, *24* (1), 101959. https://doi.org/10.1016/J.ISCI.2020.101959.

(15) Chen, G.; Wen, B.; Xie, J.-S.; Chen, L.-K.; Zhu, S.-C. Resolving the Perovskite Degradation Mechanism by Machine Learning Potential: The Case of $CsPbI_3$. *J Phys Chem C* **2023**, *127* (24), 11692–11699. https://doi.org/10.1021/ACS.JPCC.3C01589.

(16) Chen, G. Y.; Guo, Z. D.; Gong, X. G.; Yin, W. J. Kinetic Pathway of γ-to-δ Phase Transition in $CsPbI_3$. *Chem* **2022**, *8* (11), 3120–3129. https://doi.org/10.1016/j.chempr.2022.07.026.

(17) Young, J.; Rondinelli, J. M. Octahedral Rotation Preferences in Perovskite Iodides and Bromides. *J Phys Chem Lett* **2016**, *7* (5), 918–922. https://doi.org/10.1021/ACS.JPCLETT.6B00094.

(18) Dos Reis, R.; Yang, H.; Ophus, C.; Ercius, P.; Bizarri, G.; Perrodin, D.; Shalapska, T.; Bourret, E.; Ciston, J.; Dahmen, U. Determination of the Structural Phase and Octahedral Rotation Angle in Halide Perovskites. *Appl Phys Lett* **2018**, *112* (7), 071901. https://doi.org/10.1063/1.5017537.

(19) Braeckevelt, T.; Goeminne, R.; Vandenhaute, S.; Borgmans, S.; Verstraelen, T.; Steele, J. A.; Roeffaers, M. B. J.; Hofkens, J.; Rogge, S. M. J.; Van Speybroeck, V. Accurately Determining the Phase Transition Temperature of $CsPbI_3$ via Random-Phase Approximation Calculations and Phase-Transferable Machine Learning Potentials. *Chem Mater* **2022**, *34* (19), 8561–8576. https://doi.org/10.1021/ACS.CHEMMATER.2C01508.

(20) Bhatia, H.; Martin, C.; Keshavarz, M.; Dovgaliuk, I.; Schrenker, N. J.; Ottesen, M.; Qiu, W.; Fron, E.; Bremholm, M.; Van de Vondel, J.; Bals, S.; Roeffaers, M. B. J.; Hofkens, J.; Debroye, E. Deciphering the Role of Water in Promoting the Optoelectronic Performance of Surface-Engineered Lead Halide Perovskite Nanocrystals. *ACS Appl Mater Interfaces* **2023**, *15*, 7307. https://doi.org/10.1021/ACSAMI.2C20605.

(21) Protesescu, L.; Yakunin, S.; Bodnarchuk, M. I.; Bertolotti, F.; Masciocchi, N.; Guagliardi, A.; Kovalenko, M. V. Monodisperse Formamidinium Lead Bromide Nanocrystals with Bright and Stable Green Photoluminescence. *J Am Chem Soc* **2016**, *138* (43), 14202–14205. https://doi.org/10.1021/jacs.6b08900.

(22) Steele, J. A.; Solano, E.; Hardy, D.; Dayton, D.; Ladd, D.; White, K.; Chen, P.; Hou, J.; Huang, H.; Saha, R. A.; Wang, L.; Gao, F.; Hofkens, J.; Roeffaers, M. B. J.; Chernyshov, D.; Toney, M. F. How to GIWAXS: Grazing Incidence Wide Angle X-Ray Scattering Applied to Metal Halide Perovskite Thin Films. *Adv Energy Mater* **2023**, *13* (27), 2300760. https://doi.org/10.1002/AENM.202300760.

(23) Rothmann, M. U.; Lohmann, K. B.; Borchert, J.; Johnston, M. B.; McKenna, K. P.; Herz, L. M.; Nellist, P. D. Atomistic Understanding of the Coherent Interface Between Lead Iodide Perovskite and Lead Iodide. *Adv Mater Interfaces* **2023**, 2300249. https://doi.org/10.1002/ADMI.202300249.

(24) Dang, Z.; Shamsi, J.; Palazon, F.; Imran, M.; Akkerman, Q. A.; Park, S.; Bertoni, G.; Prato, M.; Brescia, R.; Manna, L. In Situ Transmission Electron Microscopy Study of Electron Beam-Induced Transformations in Colloidal Cesium Lead Halide Perovskite Nanocrystals. *ACS Nano* **2017**, *11* (2), 2124–2132. https://doi.org/10.1021/ACSNANO.6B08324.

(25) Zhu, Y.; Gui, Z.; Wang, Q.; Meng, F.; Feng, S.; Han, B.; Wang, P.; Huang, L.; Wang, H. L.; Gu, M. Direct Atomic Scale Characterization of the Surface Structure and Planar Defects in the Organic-Inorganic Hybrid $CH_3NH_3PbI_3$ by Cryo-TEM. *Nano Energy* **2020**, *73*, 104820. https://doi.org/10.1016/J.NANOEN.2020.104820.

(26) Cai, S.; Dai, J.; Shao, Z.; Rothmann, M. U.; Jia, Y.; Gao, C.; Hao, M.; Pang, S.; Wang, P.; Lau, S. P.; Zhu, K.; Berry, J. J.; Herz, L. M.; Zeng, X. C.; Zhou, Y. Atomically Resolved Electrically Active Intragrain Interfaces in Perovskite Semiconductors. *J Am Chem Soc* **2022**, *144* (4), 1910–1920. https://doi.org/10.1021/jacs.1c12235.

(27) Paul, S.; Bladt, E.; Richter, A. F.; Döblinger, M.; Tong, Y.; Huang, H.; Dey, A.; Bals, S.; Debnath, T.; Polavarapu, L.; Feldmann, J. Manganese-Doping-Induced Quantum Confinement within Host Perovskite Nanocrystals through Ruddlesden–Popper Defects. *Angew Chem Int Edit* **2020**, *59* (17), 6794–6799. https://doi.org/10.1002/ANIE.201914473.

(28) Morrell, M. V.; He, X.; Luo, G.; Thind, A. S.; White, T. A.; Hachtel, J. A.; Borisevich, A. Y.; Idrobo, J. C.; Mishra, R.; Xing, Y. Significantly Enhanced Emission Stability of $CsPbBr_3$ Nanocrystals via Chemically Induced Fusion Growth for Optoelectronic Devices. *ACS Appl Nano Mater* **2018**, *1* (11), 6091–6098. https://doi.org/10.1021/ACSANM.8B01298.

(29) Yu, Y.; Zhang, D.; Yang, P. Ruddlesden-Popper Phase in Two-Dimensional Inorganic Halide Perovskites: A Plausible Model and the Supporting Observations. *Nano Lett* **2017**, *17* (9), 5489–5494. https://doi.org/10.1021/acs.nanolett.7b02146.

(30) Yu, Y.; Zhang, D.; Kisielowski, C.; Dou, L.; Kornienko, N.; Bekenstein, Y.; Wong, A. B.; Alivisatos, A. P.; Yang, P. Atomic Resolution Imaging of Halide Perovskites. *Nano Lett* **2016**, *16* (12), 7530–7535. https://doi.org/10.1021/acs.nanolett.6b03331.

(31) Bals, S.; Van Aert, S.; Van Tendeloo, G.; Ávila-Brande, D. Statistical Estimation of Atomic Positions from Exit Wave Reconstruction with a Precision in the Picometer Range. *Phys Rev Lett* **2006**, *96* (9), 096106. https://doi.org/10.1103/PhysRevLett.96.096106.

(32) Krivanek, O. L.; Chisholm, M. F.; Nicolosi, V.; Pennycook, T. J.; Corbin, G. J.; Dellby, N.; Murfitt, M. F.; Own, C. S.; Szilagyi, Z. S.; Oxley, M. P.; Pantelides, S. T.; Pennycook, S. J. Atom-by-Atom Structural and Chemical Analysis by Annular Dark-Field Electron Microscopy. *Nature* **2010**, *464* (7288), 571–574. https://doi.org/10.1038/nature08879.

(33) Friedrich, T.; Yu, C.-P.; Verbeeck, J.; Van Aert, S. Phase Object Reconstruction for 4D-STEM Using Deep Learning. *Microsc Microanal* **2023**, *29* (1), 395–407. https://doi.org/10.1093/MICMIC/OZAC002.

(34) Ophus, C. Four-Dimensional Scanning Transmission Electron Microscopy (4D-STEM): From Scanning Nanodiffraction to Ptychography and Beyond. *Microsc Microanal* **2019**, *25* (3), 563–582. https://doi.org/10.1017/S1431927619000497.

(35) Ziatdinov, M.; Ghosh, A.; Wong, C. Y.; Kalinin, S. V. AtomAI Framework for Deep Learning Analysis of Image and Spectroscopy Data in Electron and Scanning Probe Microscopy. *Nat Mach Intell* **2022**, *4* (12), 1101–1112. https://doi.org/10.1038/s42256-022-00555-8.

(36) Yao, L.; Ou, Z.; Luo, B.; Xu, C.; Chen, Q. Machine Learning to Reveal Nanoparticle Dynamics from Liquid-Phase TEM Videos. *ACS Cent Sci* **2020**, *6* (8), 1421–1430. https://doi.org/10.1021/acscentsci.0c00430.

(37) Imran, M.; Caligiuri, V.; Wang, M.; Goldoni, L.; Prato, M.; Krahne, R.; De Trizio, L.; Manna, L. Benzoyl Halides as Alternative Precursors for the Colloidal Synthesis of Lead-Based Halide Perovskite Nanocrystals. *J Am Chem Soc* **2018**, *140* (7), 2656–2664. https://doi.org/10.1021/JACS.7B13477.

(38) Rothmann, M. U.; Li, W.; Zhu, Y.; Liu, A.; Ku, Z.; Bach, U.; Etheridge, J.; Cheng, Y. B. Structural and Chemical Changes to $CH_3NH_3PbI_3$ Induced by Electron and Gallium Ion Beams. *Advanced Materials* **2018**, *30* (25), 1–7. https://doi.org/10.1002/adma.201800629.

(39) Jain, A.; Ong, S. P.; Hautier, G.; Chen, W.; Richards, W. D.; Dacek, S.; Cholia, S.; Gunter, D.; Skinner, D.; Ceder, G.; Persson, K. A. Commentary: The Materials Project: A Materials Genome Approach to Accelerating Materials Innovation. *APL Mater* **2013**, *1* (1), 11002. https://doi.org/10.1063/1.4812323.

(40) De Backer, A.; van den Bos, K. H. W.; Van den Broek, W.; Van Aert, S. StatSTEM: An Efficient Approach for Accurate and Precise Model-Based Quantification of Atomic Resolution Electron Microscopy Images. *Ultramicroscopy* **2016**, *171* (2016), 104–116. https://doi.org/10.1016/j.ultramic.2016.08.018.

(41) De wael, A.; De Backer, A.; Lobato, I.; Van Aert, S. Modelling ADF STEM Images Using Elliptical Gaussian Peaks and Its Effects on the Quantification of Structure Parameters in the Presence of Sample Tilt. *Ultramicroscopy* **2021**, *230*, 113391. https://doi.org/10.1016/J.ULTRAMIC.2021.113391.

(42) Yaffe, O.; Guo, Y.; Tan, L. Z.; Egger, D. A.; Hull, T.; Stoumpos, C. C.; Zheng, F.; Heinz, T. F.; Kronik, L.; Kanatzidis, M. G.; Owen, J. S.; Rappe, A. M.; Pimenta, M. A.; Brus, L. E. Local Polar Fluctuations in Lead Halide Perovskite Crystals. *Phys Rev Lett* **2017**, *118* (13), 136001. https://doi.org/10.1103/PHYSREVLETT.118.136001.

(43) Yazdani, N.; Bodnarchuk, M. I.; Bertolotti, F.; Masciocchi, N.; Fureraj, I.; Guzelturk, B.; Cotts, B. L.; Zajac, M.; Rainò, G.; Jansen, M.; Boehme, S. C.; Yarema, M.; Lin, M. F.; Kozina, M.; Reid, A.; Shen, X.; Weathersby, S.; Wang, X.; Vauthey, E.; Guagliardi, A.; Kovalenko, M. V.; Wood, V.; Lindenberg, A. M. Coupling to Octahedral Tilts in Halide Perovskite Nanocrystals Induces Phonon-Mediated Attractive Interactions between Excitons. *Nat Phys* **2024**, *20* (1), 47–53. https://doi.org/10.1038/s41567-023-02253-7.

(44) Gao, M.; Park, Y.; Jin, J.; Chen, P. C.; Devyldere, H.; Yang, Y.; Song, C.; Lin, Z.; Zhao, Q.; Siron, M.; Scott, M. C.; Limmer, D. T.; Yang, P. Direct Observation of Transient Structural Dynamics of Atomically Thin Halide Perovskite Nanowires. *J Am Chem Soc* **2023**, *145* (8), 4800–4807. https://doi.org/10.1021/jacs.2c13711.

(45) Lobato, I.; van Aert, S.; Verbeeck, J. Progress and New Advances in Simulating Electron Microscopy Datasets Using MULTEM. *Ultramicroscopy* **2016**, *168*, 17–27. https://doi.org/10.1016/J.ULTRAMIC.2016.06.003.

(46) Chen, S.; Zhang, X.; Zhao, J.; Zhang, Y.; Kong, G.; Li, Q.; Li, N.; Yu, Y.; Xu, N.; Zhang, J.; Liu, K.; Zhao, Q.; Cao, J.; Feng, J.; Li, X.; Qi, J.; Yu, D.; Li, J.; Gao, P. Atomic Scale Insights into Structure Instability and Decomposition Pathway of Methylammonium Lead Iodide Perovskite. *Nat Commun* **2018**, *9* (1), 1–8. https://doi.org/10.1038/s41467-018-07177-y.